Publication Year	2022
Acceptance in OA	2025-03-10T13:47:51Z
Title	Understanding star formation in molecular clouds IV. Column density PDFs from quiescent to massive molecular clouds
Authors	Schneider, N., Ossenkopf-Okada, V., Clarke, S., Klessen, R. S., Kabanovic, S., Veltchev, T., Bontemps, S., Dib, S., Csengeri, T., Federrath, C., Di Francesco, J., Motte, F., André, Ph, Arzoumanian, D., Beattie, J. R., Bonne, L., Didelon, P., ELIA, Davide Quintino, Könyves, V., Kritsuk, A., Ladjelate, B., Myers, Ph, PEZZUTO, Stefania, Robitaille, J. F., Roy, A., Seifried, D., Simon, R., Soler, J., Ward-Thompson, D.
Publisher's version (DOI)	10.1051/0004-6361/202039610
Handle	http://hdl.handle.net/20.500.12386/36607
Journal	ASTRONOMY & ASTROPHYSICS
Volume	666

Meyerdierks, H., Heithausen, A., & Reif, K. 1991, A&A, 245, 247
Miville-Deschenes, M.-A., Martin, P., Abergel, A., et al. 2010, A&A, 518, A104
Miville-Deschenes, M.-A., Salomé, Q., Martin, P., et al. 2017, A&A, 599, A109
Minier, V., Tremblin, T., Hill, T., et al. 2013, A&A, 550, A50
Mocz, P., Burkhart, B., Hernquist, L., et al. 2017, A&A, 838, A40
Molina, F. Z., Glover, S. C. O., Federrath, C., & Klessen, R. S. 2012, MNRAS, 423, 2680
Molinari, S., Swinyard, B., Bally, J., et al. 2010, A&A, 518, A100
Motte, F., Zavagno, A., Bontemps, S., et al. 2010, A&A, 518, A77
Motte, F., Nguyen-Luong, Q., Schneider, N., et al. 2014, A&A, 571, A32
Motte, F., Bontemps, S., & Louvet, F. 2018, ARA&A, 56, 41
Myers, P. C. 2011, ApJ, 735, 82
Myers, P. C. 2015, ApJ, 806, 226
Nguyen-Luong, Q., Motte, F., Hennemann, M., et al. 2011, A&A, 535, A76
Nguyen-Luong, Q., Motte, F., Carlhoff, P., et al. 2013, ApJ, 775, 88
Nony, T., Robitaille, J. -F., Motte, F., et al. 2021, A&A, 645, A94
Nordlund, A., & Padoan, P. 1999, Interstellar Turbulence (Cambridge University Press), 218
Ossenkopf, V., & Henning, T. 1994, A&A, 291, 943
Ossenkopf, V., Krips, M., & Stutzki, J. 2008a, A&A, 485, 917
Ossenkopf, V., Krips, M., & Stutzki, J. 2008b, A&A, 485, 719
Ossenkopf-Okada, V., & Stepanov, R. 2019, A&A, 621, A5
Ossenkopf-Okada, V., Csengeri, T., Schneider, N., et al. 2016, A&A, 590, A104
Padoan, P., & Nordlund, A. A. 2002, ApJ, 576, 870
Padoan, P., Jones, J. T., & Nordlund, A. A. 1997, ApJ, 474, 730
Padoan, P., Federrath, C., Chabrier, G., et al. 2014, in Protostars and Planets VI, eds. H. Beuther, R. S. Klessen, C. P. Dullemond, & Th. Henning (University of Arizona Press)
Palmeirim, P., André, Ph., Kirk, J., et al. 2013, A&A, 550, A38
Parravano, A., Sanchez, N., & Alfaro, E. J. 2012, ApJ, 754, 150
Penston, M. V. 1969, MNRAS, 144, 425
Peretto, N., André, Ph., Könyves, V., et al. 2012, A&A, 541, A63
Peretto, N., Fuller, G. A., André, Ph., et al. 2014, A&A, 561, A83
Pezzuto, S., Elia, D., Schisano, E., et al. 2012, A&A, 547, A54
Pezzuto, S., Benedettini, M., Di Francesco, J., et al. 2021, A&A, 645, A55
Planck Collaboration Int. XXXIV. 2016, A&A, 586, A137
Poglitsch, A., Waelkens, C., Geis, N., et al. 2010, A&A, 518, A2
Pokhrel, R., Gutermuth, R. A., Ali, B., et al. 2016, MNRAS, 461, 22
Pokhrel, R., Gutermuth, R. A., Betti, S. K., et al. 2020, ApJ, 896, 60
Polychroni, D., Schisano, E., Elia, D., et al. 2013, ApJ, 777, L33
Pringle, J. E., Allen, R. J., & Lubow, S. H. 2001, MNRAS, 327, 663
Rayner, T., Griffin, M., Schneider, N., et al. 2017, A&A, 607, A22
Reach, W., Koo, B.-C., & Heiles, C. 1994, ApJ, 429, 672
Rivera-Ingraham, A., Martin, P. G., Polychroni, D., et al. 2013, ApJ, 766, 85
Roccatagliata, V., Dale, J., Ratzka, T., et al. 2015, A&A, 584, A119
Röhser, T., Kerp, J., Winkel, B., et al. 2014, A&A, 564, A71
Röllig, M., Abel, N. P., Bell, T., et al. 2007, A&A, 467, 187
Roman-Zuniga, C. G., Alves, J., Lada, C., & Lombardi, M. 2010, ApJ, 725, 2232
Roussel, H. 2013, PASP, 125, 1126
Rowles, J., & Froebrich, D. 2009, MNRAS, 395, 1640
Roy, A., Martin, P., Polychroni, D., et al. 2013, ApJ, 763, 55
Roy, A., André, Ph., Palmeirim, P., et al. 2014, A&A, 562, A138
Roy, A., André, Ph., Arzoumanian, D., et al. 2015, A&A, 584, A111
Russeil, D., Schneider, N., Anderson, L., et al. 2013, A&A, 554, A42
Russeil, D., Figueira, M., Zavagno, A., et al. 2015, A&A, 625, A134
Rygl, K. L. J., Benedettini, M., Schisano, E., et al. 2013, A&A, 549, A1
Sadavoy, S. I., Di Francesco, J., André, Ph., et al. 2012, A&A, 540, A10
Sadavoy, S. I., Di Francesco, J., André, Ph., et al. 2014, ApJ, 787, L18
Schneider, N., Bontemps, S., Simon, R., et al. 2006, A&A, 458, 855
Schneider, N., Simon, R., Bontemps, S, et al. 2007, A&A, 474, 873
Schneider, N., Csengeri T., Bontemps S., et al. 2010, A&A, 520, A49
Schneider, N., Bontemps, S., Simon, R., et al. 2011, A&A, 529, A1
Schneider, N., Csengeri, T., Hennemann, M., et al. 2012, A&A, 540, A11
Schneider, N., André, Ph., Könyves, V., et al. 2013, A&A, 766, A17
Schneider, N., Ossenkopf, V., Csengeri, T., et al. 2015a, A&A, 575, A79
Schneider, N., Csengeri, T., Klessen, R. S., et al. 2015b, A&A, 578, A29
Schneider, N., Bontemps, S., Girichidis, P., et al. 2015c, MNRAS, 453, L41
Schneider, N., Bontemps, S., Motte, F., et al. 2016, A&A, 587, A74
Schwarz, G. E. 1978, Ann. Stat., 6, 461
Seifried, D., Walch, S., Girichidis, P., et al. 2017, MNRAS, 472, 4797
Seifried, D., Haid, S., Walch, S., et al. 2020, MNRAS, 492 1465
Shu, F. H. 1977, ApJ, 214, 488
Smith, R. J., Glover, S. C. O., Bonnell, I., Clark, P., & Klessen, R. S. 2011, MNRAS, 411, 1354
Smith, R. J., Shetty, R., Beuther, H., et al. 2013 ApJ, 771, 24
Smith, R. J., Glover, S. C. O., Clark, P. C., & Klessen, R. S. 2014, MNRAS, 441, 1628
Smith, R. J., Glover, S. C. O., Klessen, R. S., & Fuller, G. A. 2016, MNRAS, 455, 3640
Soler, J. 2019, A&A, 629, A96
Spilker, A., Kainulainen, J., & Orkisz, J. 2021, A&A, 653, A63
Stanimirović, S., Murray, C. E., Lee, M.-Y., et al. 2014, ApJ, 793, 132
Sternberg, A., Le Petit, F., Roueff, E., et al 2014, ApJ, 790, 10
Stutz, A. M., & Kainulainen, J. 2015, A&A, 577, A6
Stutzki, J., Bensch, F., Heithausen, A., Ossenkopf, V., & Zielinsky, M. 1998, A&A, 336, 697
Tigé, J., Motte, F., Russeil, D., et al. 2017, A&A, 602, A77
Tremblin, P., Audit, E., Minier, V., et al. 2012a, A&A, 538, A31
Tremblin, P., Audit, E., Minier, V., et al. 2012b, A&A, 546, A33
Tremblin, P., Minier, V., Schneider, N., et al. 2013, A&A, 560, A19
Tremblin, P., Schneider, N., Minier, V., et al. 2014, A&A, 564, A106
Valdivia, V., Hennebelle, P., Gérin, M., Lesaffre, P. 2016, A&A, 587, A76
Vazquez-Semadeni, E. 1994, ApJ, 423, 681
Vázquez-Semadeni, E., & Garcia, N. 2001, ApJ, 557, 727
Veltchev, T. V., Donkov, S, Klessen, & R. S. 2016, MNRAS, 459, 2432
Veltchev, T. V., Girichidis, P., Donkov, S., et al. 2019, MNRAS, 489, 788
Virkar, Y., & Clauset, A. 2014, Ann. Appl. Stat., 8, 8
Visser, R., van Dishoeck, E. F., & Black, J. H. 2009, A&A, 503, 323
Ward, R. L., Wadsley, J., & Sills, A. 2014, MNRAS, 445, 1575
Ward-Thompson, D., Kirk, J., André, Ph., et al. 2010, A&A, 518, L92
Whitworth, A., & Summers, D. 1985, MNRAS, 214, 1
Winkel, B., Kerp, J., Kalberla, P., et al. 2016, A&A, 585, A41
Wolfire, M. G., Hollenbach, D., & McKee, C. F. 2010, ApJ, 716, 1191
Zari, E., Lombardi, M., Alves, J., et al. 2016, A&A, 587, A106
Zucker, C., Goodman, A. A., Alves, J., et al. 2020, A&A, 633, A51

Appendix A: Line-of-sight contamination correction

In Ossenkopf et al. (2016), we simulated the effect of LOS contamination on the column-density N-PDF of a molecular cloud assuming a contamination by a typical diffuse cloud that has a total column density below that of the investigated molecular cloud, but a spread in column densities that may be wider. We found that the underlying N-PDF of the observed cloud can be approximately restored from the observations by treating the contamination like a constant screen, systematically shifting the column densities. As this is only a first-order correction, we also provided estimates for the residual change of the N-PDF parameters in terms of the peak position and the N-PDF width in case of a log-normal distribution.

For many clouds in this paper, we are in a somewhat different regime. The contamination is given by the Galactic structure that provides a larger column density but is more homogeneous on the scale of the individual molecular clouds. Hence, we repeat here the computations from Ossenkopf et al. (2016) for an adjusted parameter range. Here, we allow for contaminations of up to four times the typical column density of the considered cloud, but the contaminating cloud has a lower spread in its N-PDF width of at most half that for the considered cloud. This new regime covers all configurations from this paper.

We first illustrate the LOS-contamination correction using the example of the Aquila cloud and then validate the results. We note that we used Method 1 here for the fitting so that the derived values are slightly different to what was obtained with Method 4. Figure A.1 shows the uncorrected Aquila column density map and the rectangular subregion with the lowest level of emission that we consider to be a measure for the contamination level. The mean of the pixel values inside this latter area is $A_V = 2.5$. From these pixels, we obtained the N-PDF of the contamination. In the Aquila case, this area has 468×350 pixels on a $5.8''$ grid, which was sufficient to obtain a reliable N-PDF. For all other clouds, we had similar contamination sample sizes. Most of the N-PDFs show a clear log-normal distribution like Aquila, and only in Serpens we did obtain an additional PLT. Figure A.2 (top) displays the N-PDFs of Aquila obtained from the original (LOS-uncorrected) column density map. The middle panel shows the N-PDF constructed from the pixels in the rectanglur subregion, and on the bottom the final N-PDF derived from the LOS-corrected map (using a constant value of $A_V = 2.5$) is displayed. The peak value and width of the contaminated N-PDF are then used to calculate the ratios $\sigma_{\eta,cont}/\sigma_{\eta,cloud}$ and $N_{contam}/N_{\rm peak}$ to assesss if the removal of a constant value is an adequate choice, following Ossenkopf et al. (2016). The ratio $\sigma_{\eta,\rm cont}/\sigma_{\eta,\rm cloud}$ for Aquila is 0.19, the highest value for all clouds, and the ratio $N_{contam}/N_{\rm peak}$ is 0.82. We note that the normalization of the N-PDF differs between Paper I and Ossenkopf et al. (2016). While Paper I uses the normalization $\eta \equiv \ln\frac{N}{\langle N\rangle}$, Ossenkopf et al. (2016) take the logarithmic peak N_{peak} for log-normal distributions as they center them at $\eta = 0$. The relation between the two normalizations is $N_{peak}(N) = \langle N\rangle\ \exp(-1.5\,\sigma_\eta^2)$.

Figures A.3 and A.4 show the results equivalent to Figs. 13 and 14 from Ossenkopf et al. (2016), respectively. Figure A.3 displays the distribution of resulting N-PDFs obtained when convolving a log-normal cloud N-PDF with a second log-normal "contaminating" N-PDF and subsequently correcting this contamination by subtracting a constant N_{contam} contamination column density. Each vertical line in the plot represents one reconstructed N-PDF. The horizontal axis gives the dependence on the ratio between the contamination and the cloud column densities N_{contam}/N_{peak}. Here, the cloud and contamination column densities, N_{peak} and N_{contam}, denote the most probable column density on a logarithmic scale, providing the peaks of the log-normal N-PDFs. In this example, the width of the cloud N-PDF was assumed to be $\sigma_{\eta,cloud} = 0.5$ and the width of the contamination $\sigma_{\eta,cont} = 0.15$. The distribution at the left edge represents the original cloud N-PDF because it was computed for a contamination and correction with $N_{contam} = 0$. Like in Ossenkopf et al. (2016), we find a good reproduction of the central part of the original N-PDF for the whole range of contamination amplitudes but a shift of the N-PDF peak position by up to $\Delta\eta = 0.35$. Moreover, there is a residual broadening of the distribution, in particular toward lower column densities where the N-PDF becomes shallower. The logarithmic scale used in the plot, however, strongly emphasizes these deviations. They actually occur at levels of less than 1 % of the N-PDF peak.

For the description of these residuals after the constant screen correction, we also extended the parameter scan from Ossenkopf et al. (2016) over the full parameter range $N_{contam}/N_{peak} = 0\ldots4$ and $\sigma_{\eta,cont}/\sigma_{eta,cloud} = 0\ldots0.5$. Figure A.4 shows the results. The shift of the peak of the N-PDF, shown in the upper plot, goes up to a factor of 2 in column density for strong contaminations with a large width. The lower plot shows the broadening of the distribution relative to the original cloud value. With these cases in hand, we can look up the most extreme cases from our cloud sample.

Summarizing, a LOS-correction has a clear influence on the N-PDF parameters and needs to be considered before all further analysis. In the Aquila case, the PLT slope changes from a rather steep one (-2.67) to a flatter one (-2.14). Earlier estimates of the slope of the uncorrected column density also obtained steep PLTs with a slope of -2.59 (Schneider et al. 2013) and -2.9 (Könyves et al. 2015). The width of the N-PDF increases from $\eta = 0.30$ to 0.35 and the DP moves from $A_V = 8.1$ to 4.6.

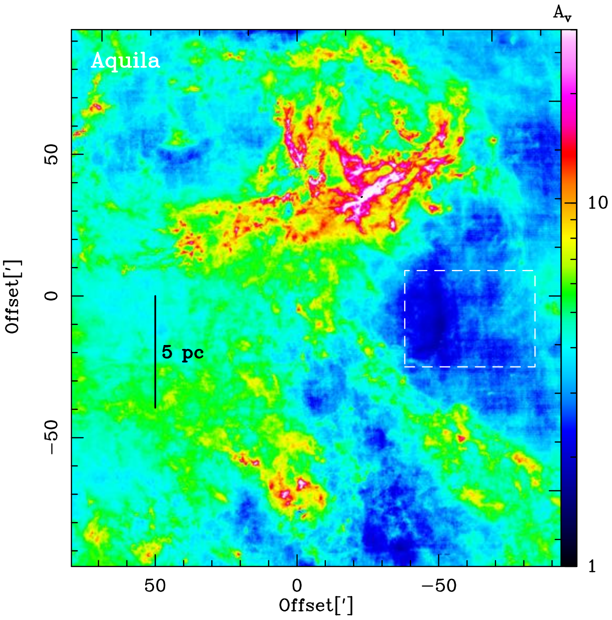

Fig. A.1: LOS-uncorrected column density of the Aquila cloud expressed in visual extinction. The white dashed rectangle indicates the region used for evaluating the LOS-contamination by (i) taking the mean of all pixels inside the rectangle ($A_V = 2.5$) and (ii) constructing an N-PDF from these pixels and determining the peak of the distribution ($A_V = 2.4$, see Figure A.2).

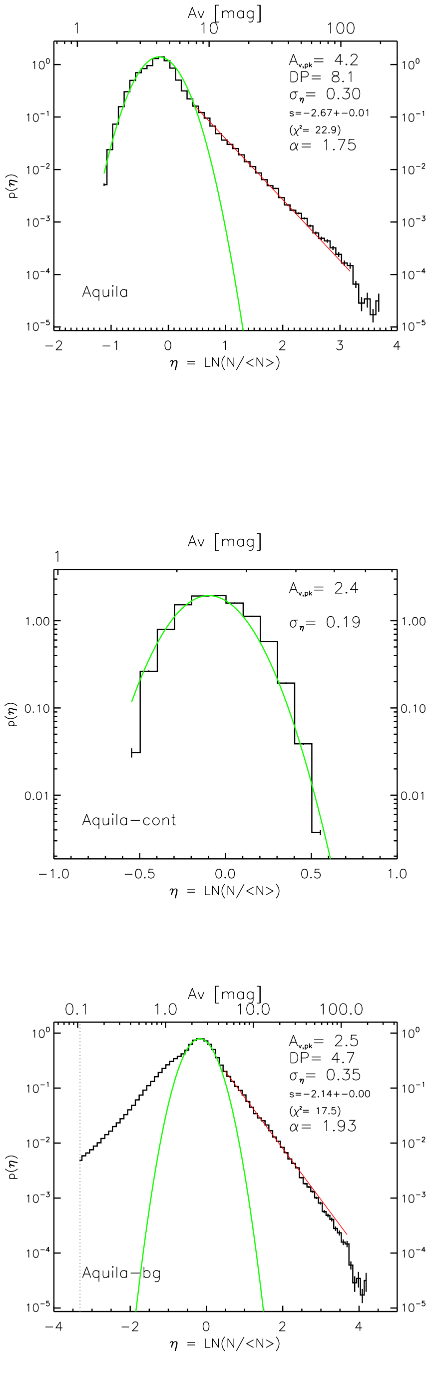

Fig. A.2: N-PDFs obtained from the LOS-uncorrected column density map (top), from the pixels within the white rectangle from Fig. A.1 (middle), and from the LOS-corrected column density map (bottom).

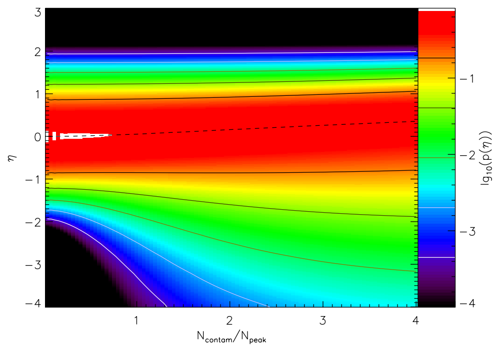

Fig. A.3: Two-dimensional representation of the N-PDFs of contaminated clouds after applying the constant screen correction as a function of the ratio between the contamination strength N_{contam} and the typical cloud column density N_{peak}. The width of the cloud N-PDF was assumed to be $\sigma_{\eta,cloud}$ = 0.5 and the width of the contamination $\sigma_{\eta,cont}$ = 0.15, using some typical values for the clouds in this paper. The N-PDFs are represented through colors showing the logarithm.

Appendix B: Significance of fitted models and slope comparison

Appendix B.1. BIC information

Tables B.1 and B.2 give the Bayesian information criterion (BIC) values and the weights, respectively, for the clouds in the study that were analyzed with method 4. The most likely model is the one with the lowest BIC values and the ratios of the weights gives a measure of how favored a model is compared to another. There are some models with a weight of 0 because it is just so low.

Appendix B.2. Comparison between different slope determinations

As pointed out in Sec. 2.4.1, the three methods used to fit the N-PDF differ in their premises. In contrast to Methods 1 and 2, the adapted BPLFIT technique (Method 3, see Veltchev et al. (2019) extracts possible PLTs, without any assumption on the rest of the distribution. Marinkova et al. (2021) modified this technique further – through introduction of varying lower and upper density cutoffs – to allow for extraction of a second PLT.

It is therefore instructive to compare the slopes obtained through Method 3 with those from the other two. In general, the BPLFIT slopes correlate well with their counterparts. Method 2 extracts only single PLTs but some of them are identified with the first PLT (with a single exception) obtained through Method 3 (right panel). A few more significant discrepancies are due to differences between the estimated DPs. Methods 1 and 3 agree on the existence of two PLTs in eight studied regions of all types, with a good agreement between the obtained slope values (open squares in the left panel). For the rest of the regions, the first PLTs from Method 1 are typically identified with single PLTs extracted by Method 3 (filled triangles). The correlation between the slope values is even better than in the regions for which both techniques extract two PLTs.

Appendix C: Column density maps, N-PDFs and Δ-variance spectra

Figures C.1-C.29 display the column density maps expressed in visual extinction on the left and the Δ-variance and N-PDF on the right. The plot range is 0.5 to 200 in A_V for high-mass SF

Table B.1: Bayesian information criterion values for all clouds and for all models. The model with the minimum BIC is shown in bold. We note that for Draco, no PLT could be fit, the most likely model is the ELL one with a BIC of -382.2. Other models (EL, L, LL, LP etc.) have higher BICs.

Model	ELP	ELLP	EL2P	ELL2P	LP	LLP	L2P	LL2P
High-mass SF regions								
Cygnus North	-503.88	-871.82	-719.87	**-914.78**	8671.25	41.67	8300.31	-174.01
Cygnus South	-309.28	-608.02	-318.54	**-617.44**	11267.88	715.80	9802.92	707.52
M16	23.91	**-536.85**	-123.23	-406.03	1210.30	-307.46	1045.74	-190.63
M17	4356.28	264.01	3212.22	**98.91**	23378.30	5528.30	19586.52	5642.49
NGC6334	8063.80	-236.74	7851.92	**-542.82**	61030.20	3553.64	51465.35	3469.84
NGC6357	3563.59	-226.32	3541.21	**-250.39**	14412.52	6246.08	11648.62	4234.76
NGC7538	483.82	71.95	25.69	**-64.33**	2687.11	607.64	1798.76	601.15
Rosette	-92.52	-518.24	-416.58	**-546.29**	1293.80	167.18	1033.42	175.69
Vela C	575.47	-105.57	116.86	**-352.96**	8364.11	1178.53	2497.10	87.91
Intermediate-mass SF regions								
Aquila	-283.75	-618.65	-415.31	**-749.90**	15509.10	991.36	13294.37	890.44
MonR2	221.51	-65.93	-447.38	**-503.61**	8809.96	-299.52	7972.57	-410.60
MonOB1	4339.68	116.11	4239.46	**-176.29**	10159.28	774.17	10044.87	311.15
NGC2264	277.97	216.35	216.46	**75.87**	10524.29	745.90	10105.42	1106.19
Orion B	149.43	86.70	-470.14	**-542.29**	144.98	129.05	-474.24	-492.82
Serpens	1099.54	145.28	546.30	**90.14**	23029.18	2674.87	19708.70	2617.06
Low-mass SF regions								
ChamI	9394.67	372.33	**134.39**	217.27	43476.62	1435.52	3104.40	1321.47
ChamII	404.72	-264.60	324.52	**-361.85**	9221.02	-148.55	7.01	-237.61
IC5146	2062.21	1964.76	216.23	**-365.36**	2258.17	2058.07	339.46	-265.88
Lupus I	117.50	75.00	-23.75	**-36.72**	16701.75	423.47	1761.06	542.80
Lupus III	208.33	-160.58	-103.01	**-178.68**	280.77	-43.10	-22.35	-116.40
Lupus IV	-113.56	-366.87	-320.08	**-425.10**	47.10	-145.50	-46.51	-350.43
Perseus	155.23	-359.51	-446.61	-441.65	1419.38	-330.10	**-454.69**	-442.44
Pipe	-152.55	-311.61	-320.53	**-375.61**	-156.14	-281.39	-304.53	-376.78
ρOph	12934.22	12189.37	450.90	-248.50	12928.56	12182.47	443.59	**-254.23**
Taurus	2085.79	2079.25	-290.70	-352.77	2314.11	2026.09	-99.35	**-356.92**
Quiescent regions								
ChamIII	109.96	-470.85	5.27	**-487.08**	273.33	-317.40	-3.95	-333.85
Musca	3406.39	-347.94	-307.86	-350.00	8338.84	-180.95	-221.75	**-352.48**
Polaris	-245.60	-353.62	-258.46	**-359.30**	-194.85	-315.35	-217.47	-318.71

molecular clouds. Since all these clouds are affected by LOS contamination, we show the corrected column density maps and N-PDFs. The plot range for intermediate-mass SF clouds is 0.5 to 100 in A_V, for low-mass SF clouds 0.1 to 20 in A_V, for quiescent clouds 0.1 to 10 in A_V, and for Draco 0.1 to 2 in A_V. The N-PDFs are presented as they are without the fits to the log-normal part and PLT(s). These are shown separately in Appendix D. As outlined in Sec. 2.4, the values of the slope(s) of the PLT(s), the DP and the width of the log-normal part are taken from the fit of method 4.

Table B.2: Bayesian information criterion weight values for all clouds and for all models. The most likely model is denoted by its weight being bold. If the second most likely model has a weight within a factor of 10 of the most likely model (i.e. may be an alternative model) it is shown with an italic, bold weight. We note that for Draco, no PLT could be fit, the most likely model is the ELL one with a weight of 9.826514e-01. Other models (EL, L, LL, LP etc.) have higher weights.

Model	ELP	ELLP	EL2P	ELL2P	LP	LLP	L2P	LL2P
High-mass SF regions								
Cygnus North	5.946e-90	4.692e-10	4.741e-43	**1.000e+00**	0.000e+00	2.039e-208	0.000e+00	1.393e-161
Cygnus South	1.202e-67	8.924e-03	1.233e-65	**9.911e-01**	0.000e+00	3.067e-290	0.000e+00	1.926e-288
M16	1.708e-122	**1.000e+00**	1.526e-90	3.916e-29	0.000e+00	1.544e-50	0.000e+00	6.596e-76
M17	0.000e+00	1.409e-36	0.000e+00	**1.000e+00**	0.000e+00	0.000e+00	0.000e+00	0.000e+00
NGC6334	0.000e+00	3.432e-67	0.000e+00	**1.000e+00**	0.000e+00	0.000e+00	0.000e+00	0.000e+00
NGC6357	0.000e+00	5.933e-06	0.000e+00	**1.000e+00**	0.000e+00	0.000e+00	0.000e+00	0.000e+00
NGC7538	9.348e-120	2.554e-30	2.834e-20	**1.000e+00**	0.000e+00	1.212e-146	0.000e+00	3.111e-145
Rosette	2.911e-99	8.076e-07	6.816e-29	**9.999e-01**	0.000e+00	1.177e-155	0.000e+00	1.665e-157
Vela C	2.477e-202	1.905e-54	9.547e-103	**1.000e+00**	0.000e+00	0.000e+00	0.000e+00	1.846e-96
Intermediate-mass SF regions								
Aquila	5.982e-102	3.158e-29	2.212e-73	**1.000e+00**	0.000e+00	0.000e+00	0.000e+00	0.000e+00
MonR2	3.485e-158	9.099e-96	6.163e-13	**1.000e+00**	0.000e+00	4.813e-45	0.000e+00	6.355e-21
MonOB1	0.000e+00	3.207e-64	0.000e+00	**1.000e+00**	0.000e+00	4.076e-207	0.000e+00	1.425e-106
NGC2264	1.302e-44	3.127e-31	2.960e-31	**1.000e+00**	0.000e+00	3.198e-146	0.000e+00	1.857e-224
Orion B	6.236e-151	2.609e-137	2.152e-16	**1.000e+00**	5.771e-150	1.661e-146	1.672e-15	1.810e-11
Serpens	6.480e-220	1.063e-12	8.833e-100	**1.000e+00**	0.000e+00	0.000e+00	0.000e+00	0.000e+00
Low-mass SF regions								
ChamI	0.000e+00	2.148e-52	**1.000e+00**	1.007e-18	0.000e+00	2.905e-283	0.000e+00	1.694e-258
ChamII	3.479e-167	7.628e-22	9.050e-150	**1.000e+00**	0.000e+00	4.814e-47	8.000e-81	1.051e-27
IC5146	0.000e+00	0.000e+00	5.121e-127	**1.000e+00**	0.000e+00	0.000e+00	8.918e-154	2.501e-22
Lupus I	3.243e-34	5.491e-25	1.524e-03	**9.985e-01**	0.000e+00	1.176e-100	0.000e+00	1.439e-126
Lupus III	9.158e-85	1.174e-04	3.702e-17	**9.999e-01**	1.705e-100	3.623e-30	1.131e-34	2.992e-14
Lupus IV	2.238e-68	2.267e-13	1.567e-23	**1.000e+00**	2.905e-103	1.930e-61	6.169e-83	6.104e-17
Perseus	3.530e-133	2.099e-21	1.725e-02	1.444e-03	0.000e+00	7.782e-26	**9.792e-01**	2.134e-03
Pipe	1.308e-49	4.531e-15	3.919e-13	***3.578e-01***	7.876e-49	1.242e-21	1.315e-16	**6.422e-01**
Taurus	0.000e+00	0.000e+00	3.708e-15	***1.116e-01***	0.000e+00	0.000e+00	1.042e-56	**8.884e-01**
Quiescent regions								
ChamIII	2.261e-130	2.989e-04	1.223e-107	**9.997e-01**	7.567e-166	1.427e-37	1.229e-105	5.326e-34
Musca	0.000e+00	7.418e-02	1.469e-10	***2.078e-01***	0.000e+00	4.063e-38	2.941e-29	**7.180e-01**
Polaris	1.931e-25	5.520e-02	1.197e-22	**9.448e-01**	1.843e-36	2.702e-10	1.504e-31	1.450e-09

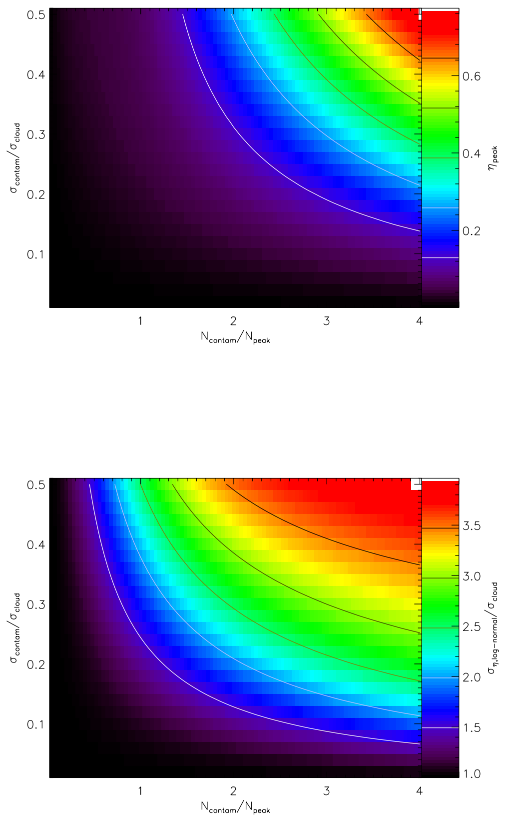

Fig. A.4: Parameters of the N-PDFs of contaminated clouds corrected for the contamination through the subtraction of a constant offset given by the peak of the N-PDF of the contaminating structure. The upper plot shows the position of the N-PDF peak on the logarithmic column density scale η relative to the original peak column of the cloud. Consequently a value of 0 represents the correct peak position; a value of 0.5 indicates a 65 % overestimate of the column. The lower plot shows the width of the corrected cloud N-PDF relative to the original cloud N-PDF. On the horizontal axis, we varied the amplitude of the contamination, while on the vertical axis its width relative to the cloud N-PDF width.

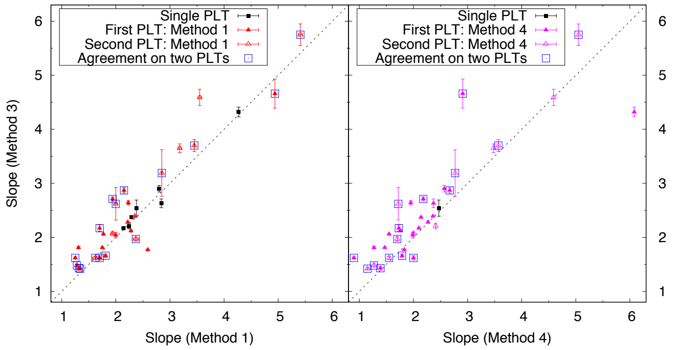

Fig. B.1: Comparison of slope estimations from the three PLTs fitting methods described in Sec. 2.4.1. Absolute slope values are given and the identity line is plotted as a dashed line. Different symbols are used for one or two PLTs. We note that the methods do not always agree on the number of PLTs.

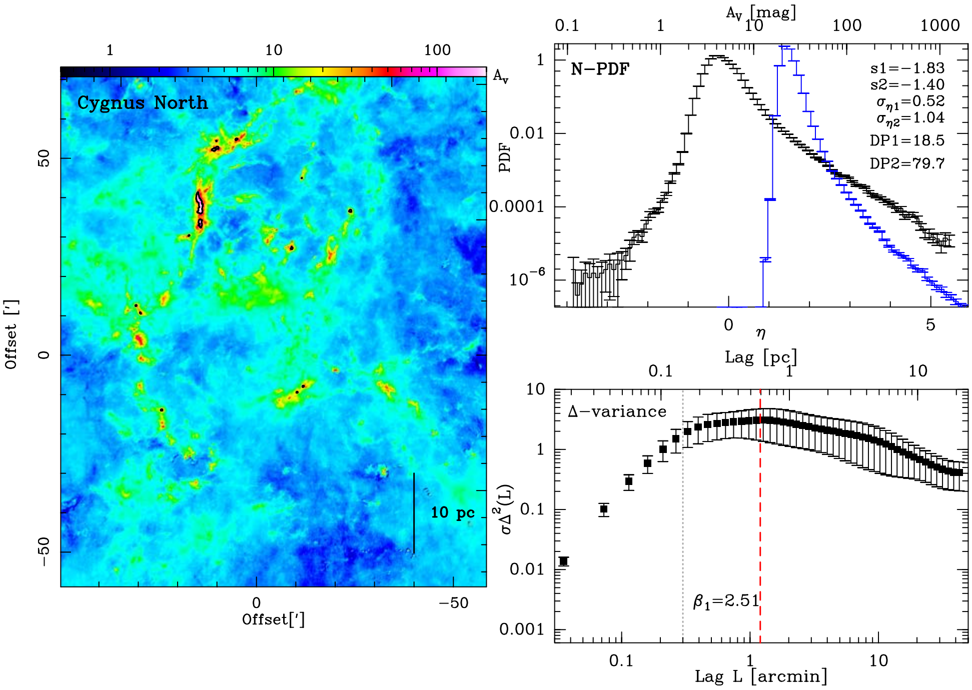

Fig. C.1: CYGNUS X NORTH (DR21): **Left:** LOS corrected column density map in visual extinction. The image is rotated and a length scale is given in the panel. For the cloud N-PDFs with two PLTs, the contour of the second DP is plotted in black. **Right (lower panel):** Δ-variance spectrum. X-axis units are arcmin (bottom) and parsec (top). The black dashed line indicates the angular resolution (18″), the first red dashed line indicates the upper limit for the fit of β_1 (the lower limit is the resolution limit) and in case there are two fitting intervalls, two other red dashed lines indicate the fit range for β_2. The values of β_1 and β_2 are given in the panel. The errors are omitted for better visibility, they are always on the order of 0.01 to 0.03. **Right (top panel):** N-PDF of LOS corrected column density in black, expressed in visual extinction (upper x-axis) and in η (lower x-axis). For comparison, the N-PDF of the uncorrected map is displayed in blue. The slope s of the PLT, the width σ (expressed in η) of the log-normal part of the (corrected) N-PDF, and the deviation point DP (expressed in A_V) are given in the panel.

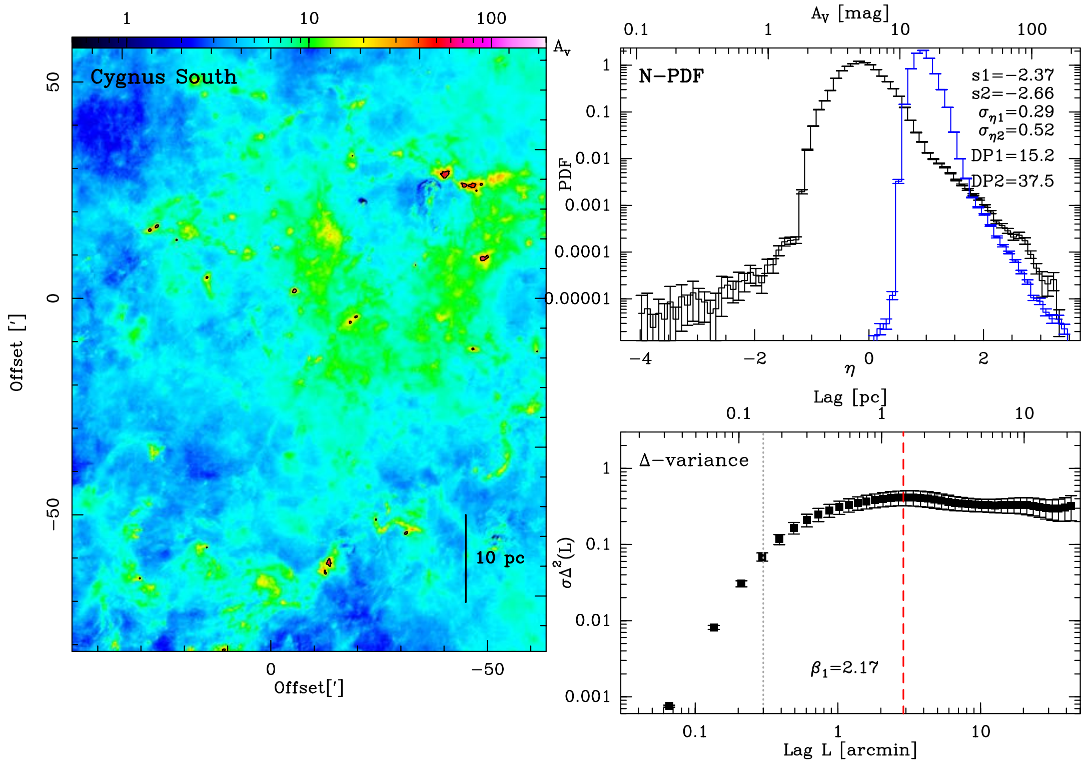

Fig. C.2: CYGNUS X SOUTH (DR15): Fig. caption see Fig. C.1.

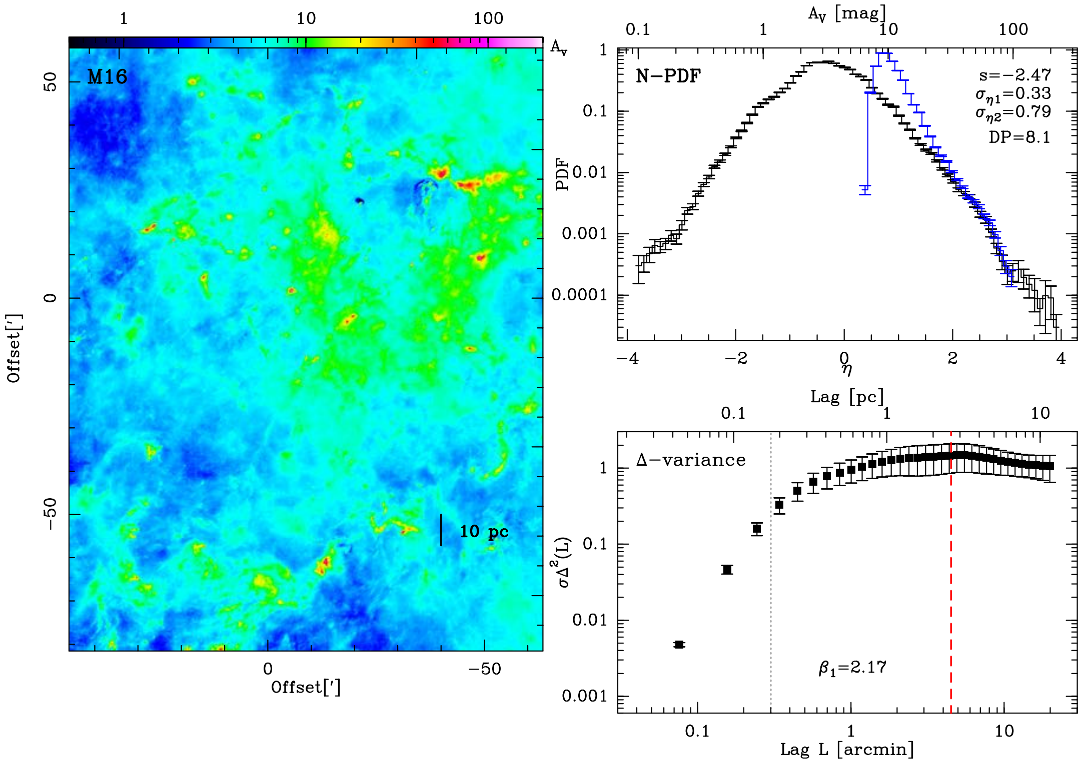

Fig. C.3: M16: Fig. caption see Fig. C.1.

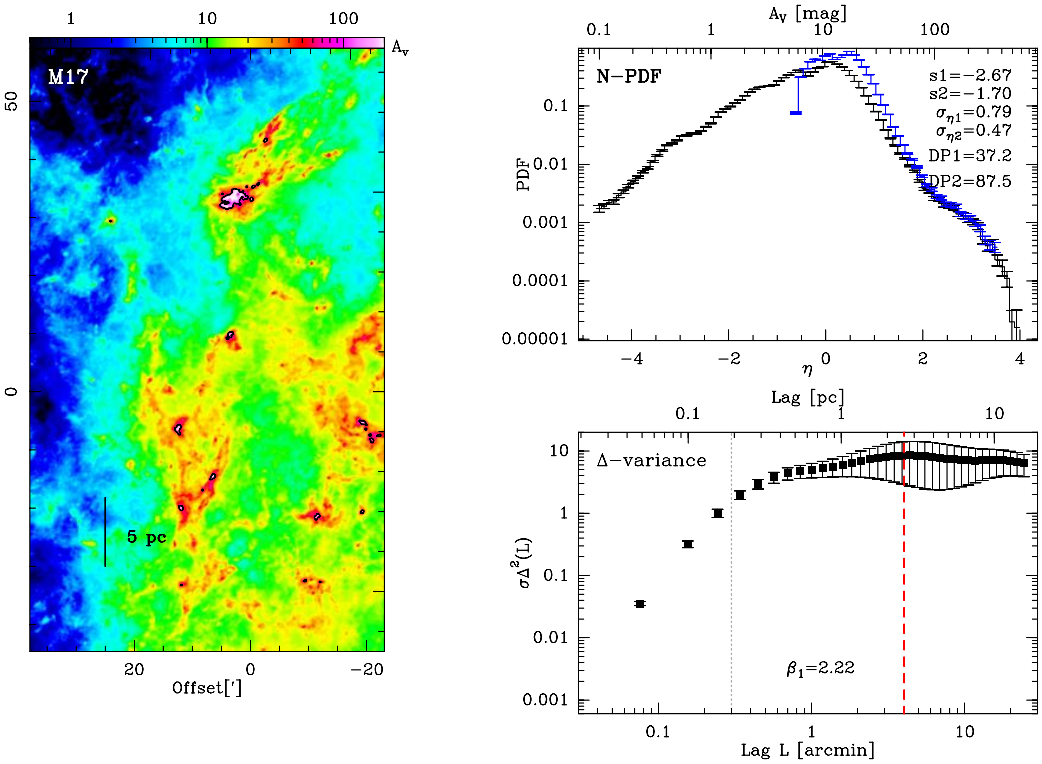

Fig. C.4: M17: Fig. caption see Fig. C.1.

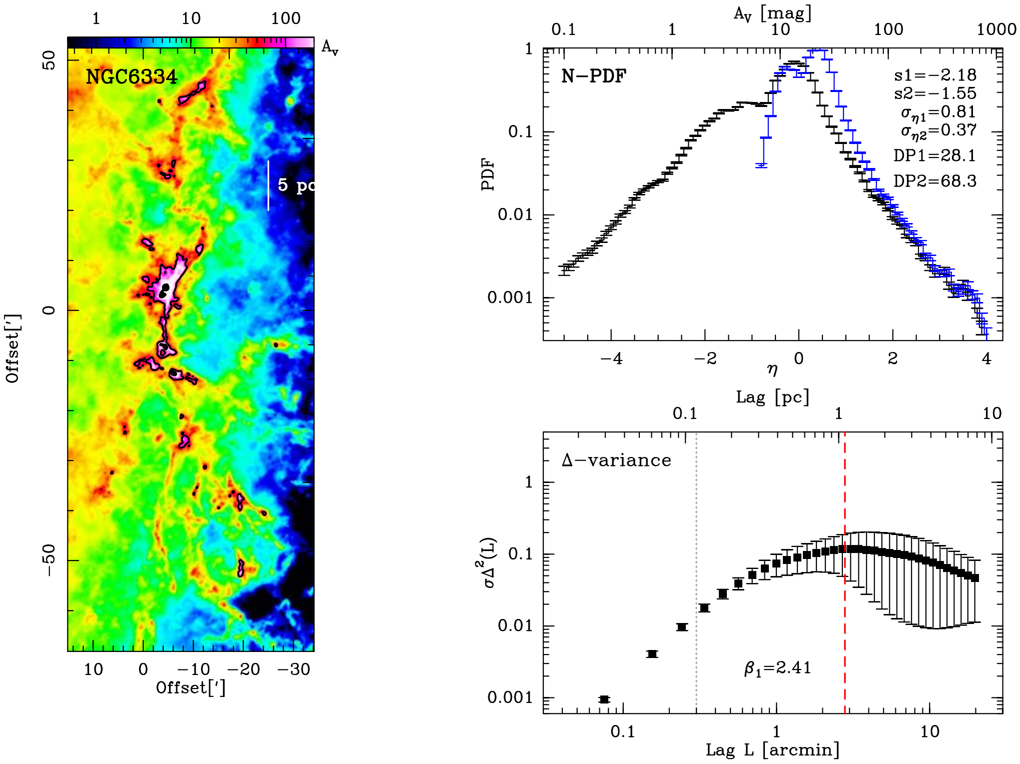

Fig. C.5: NGC6334: Fig. caption see Fig. C.1.

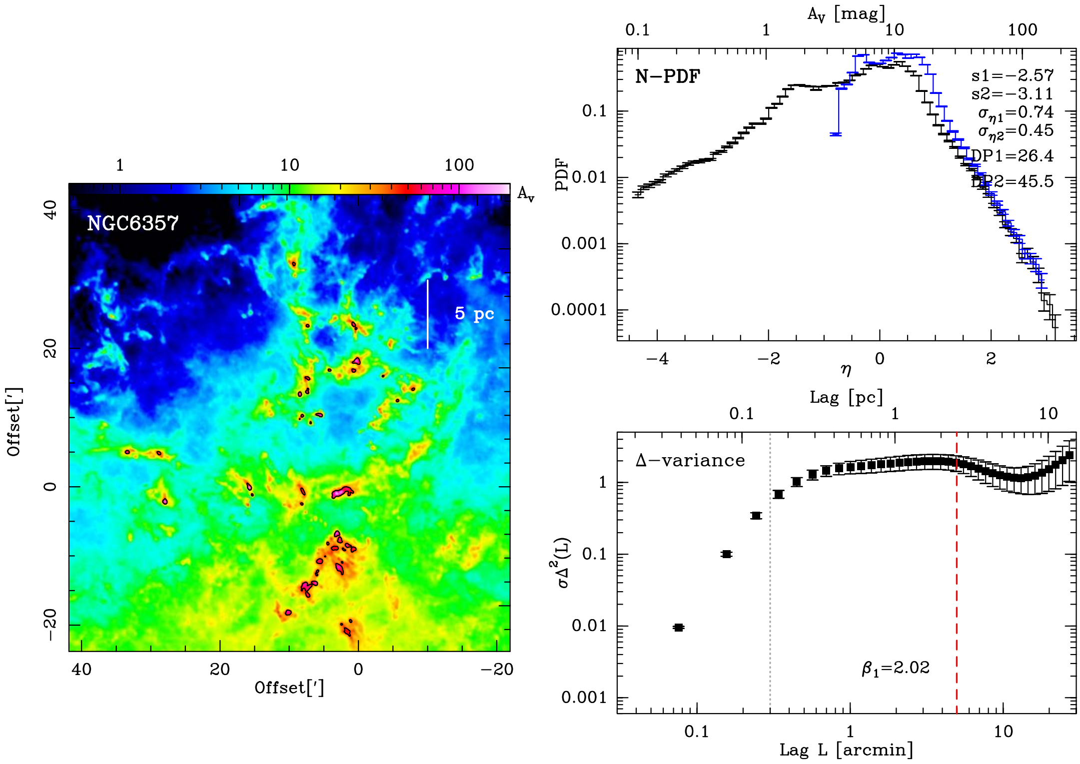

Fig. C.6: NGC6357: Fig. caption see Fig. C.1.

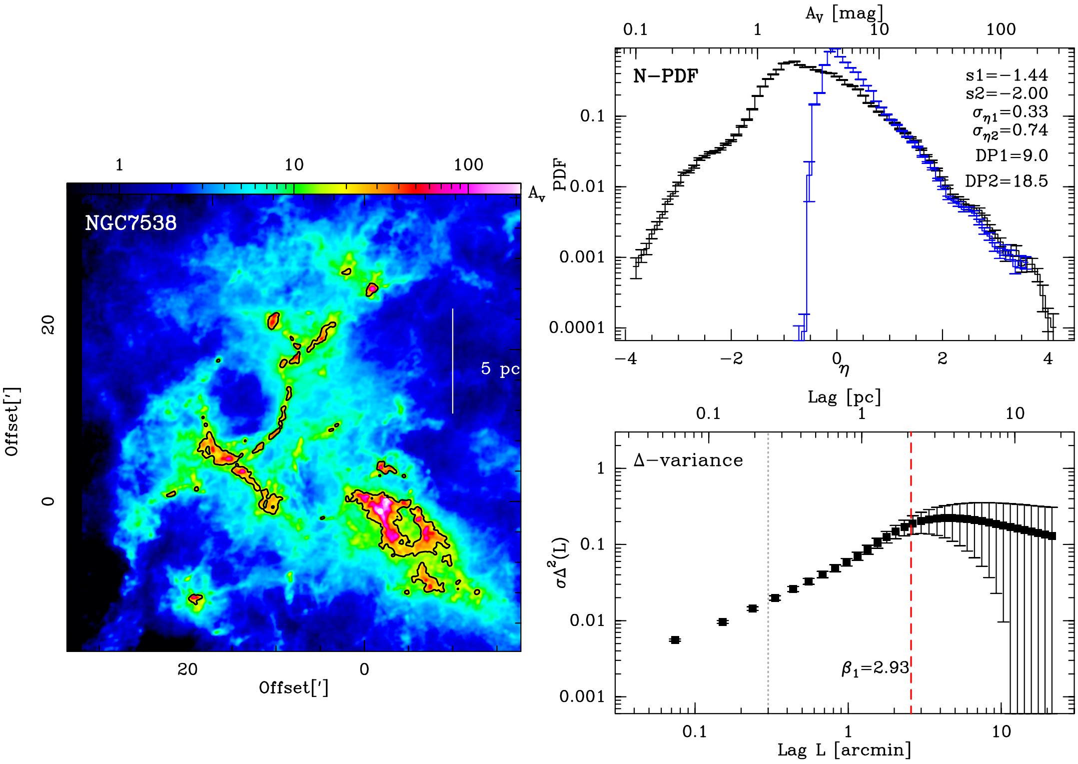

Fig. C.7: NGC7538: Fig. caption see Fig. C.1.

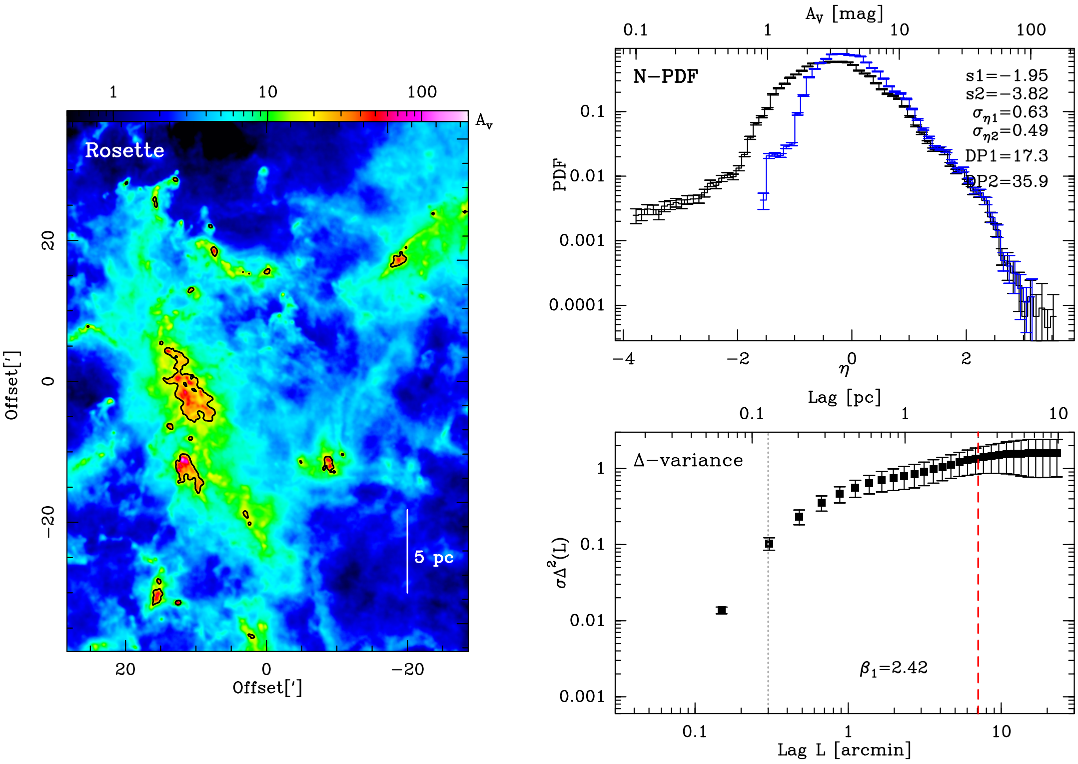

Fig. C.8: ROSETTE: Fig. caption see Fig. C.1.

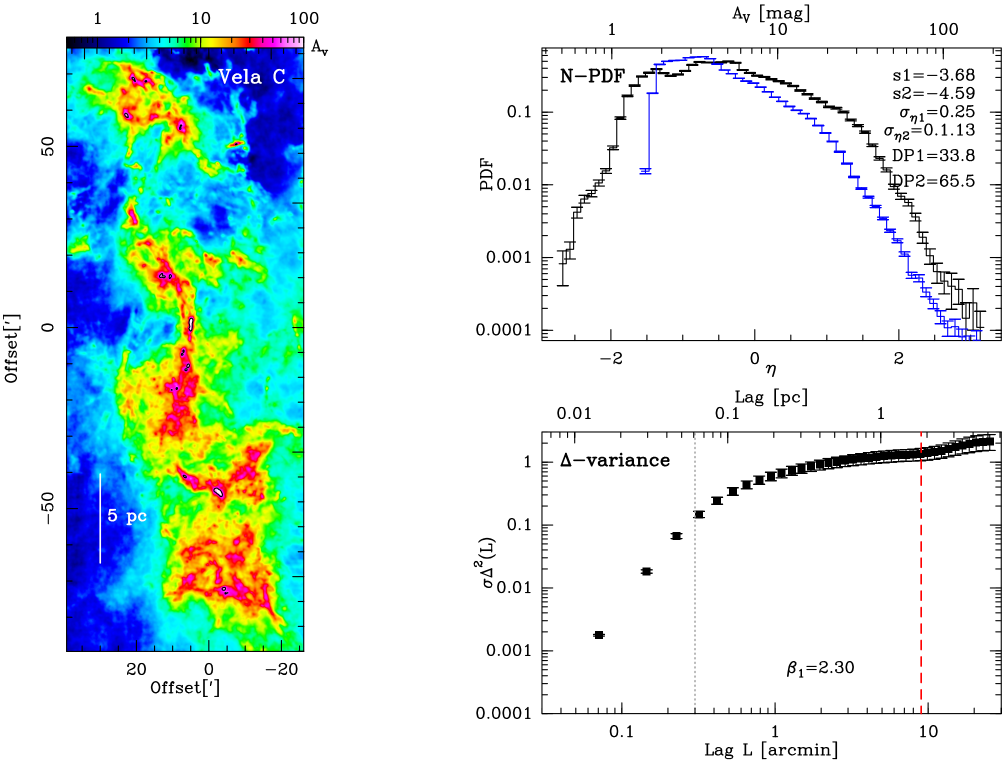

Fig. C.9: VELA C: Fig. caption see Fig. C.1.

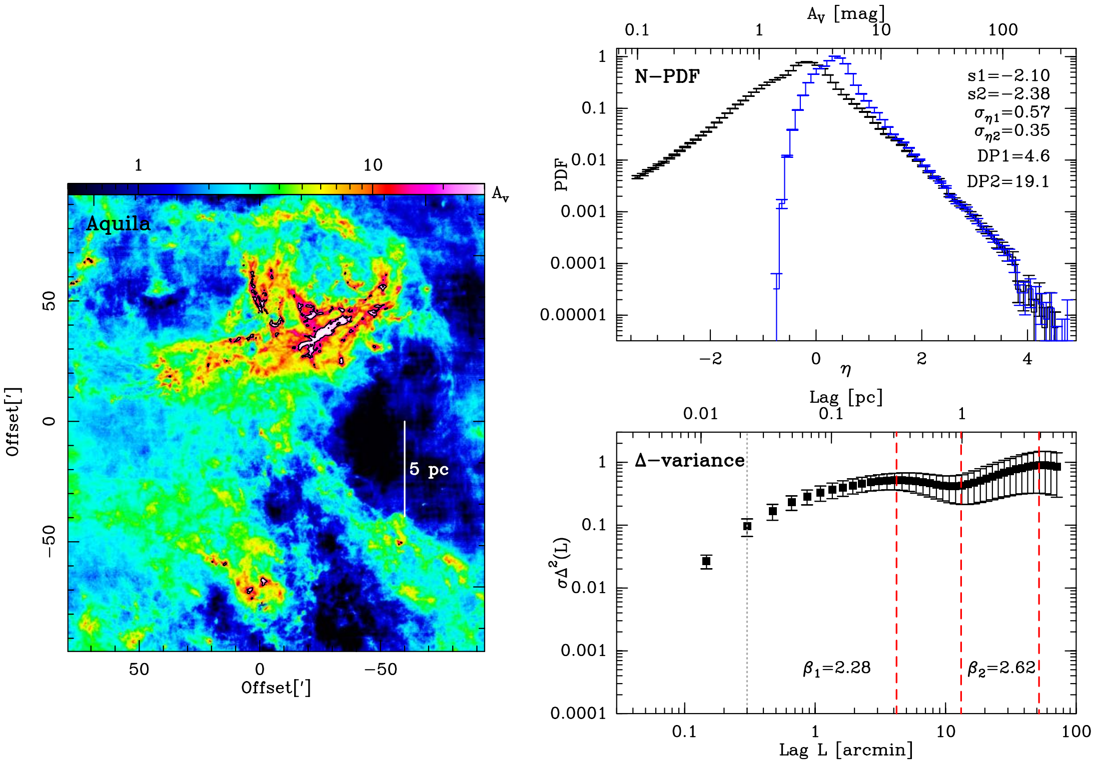

Fig. C.10: AQUILA: Fig. caption see Fig. C.1.

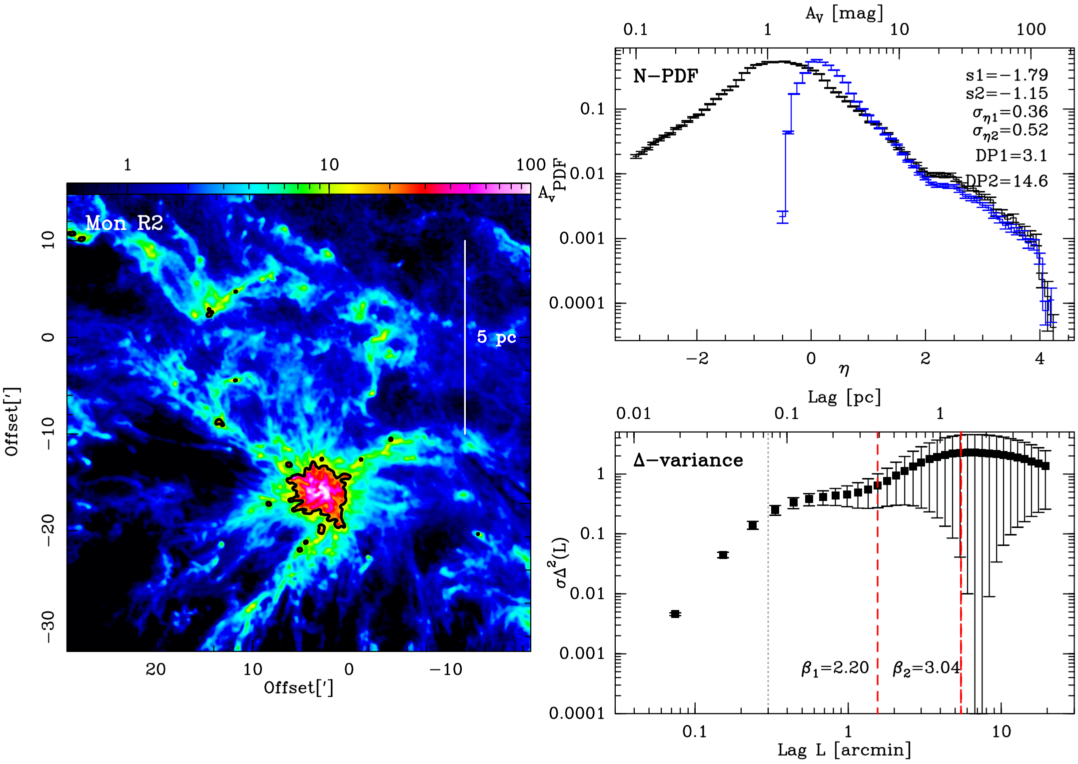

Fig. C.11: MONR2: Fig. caption see Fig. C.1.

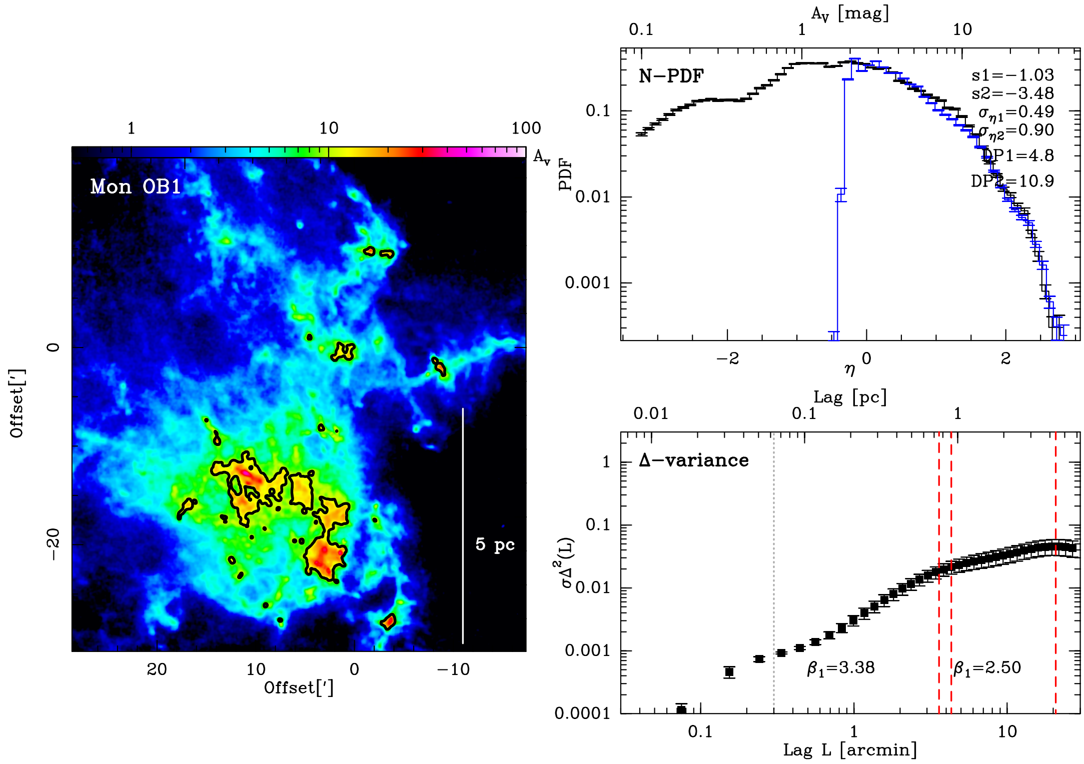

Fig. C.12: MONOB1: Fig. caption see Fig. C.1.

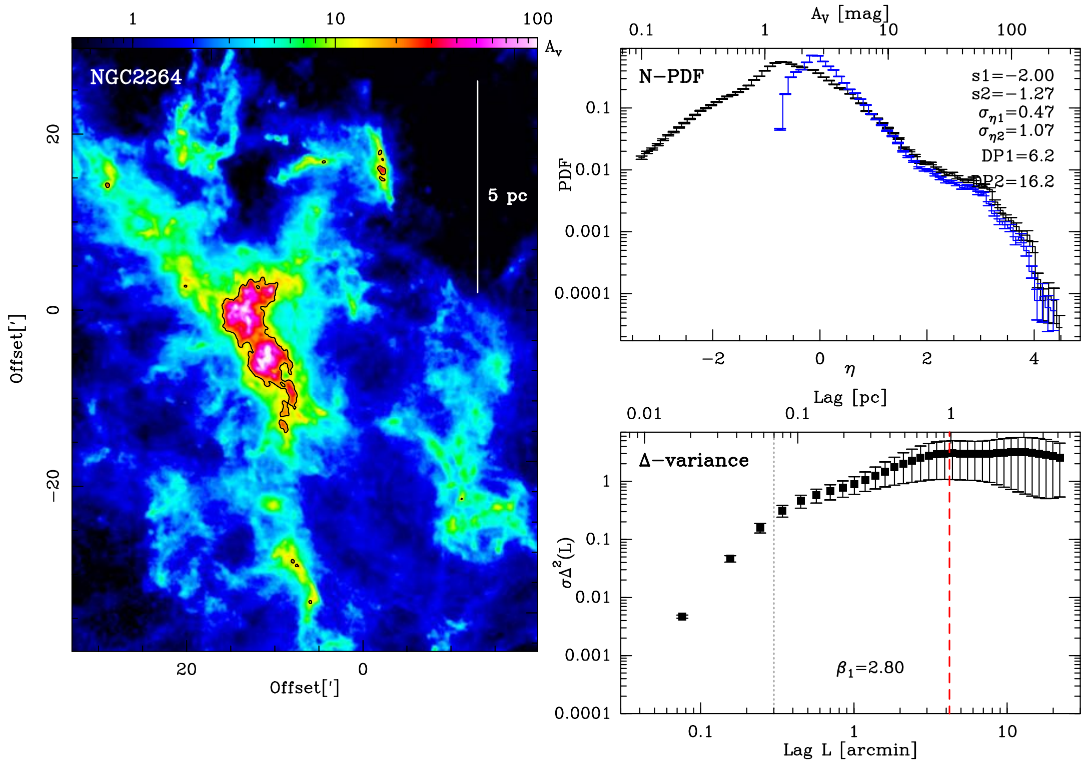

Fig. C.13: NGC2264: Fig. caption see Fig. C.1.

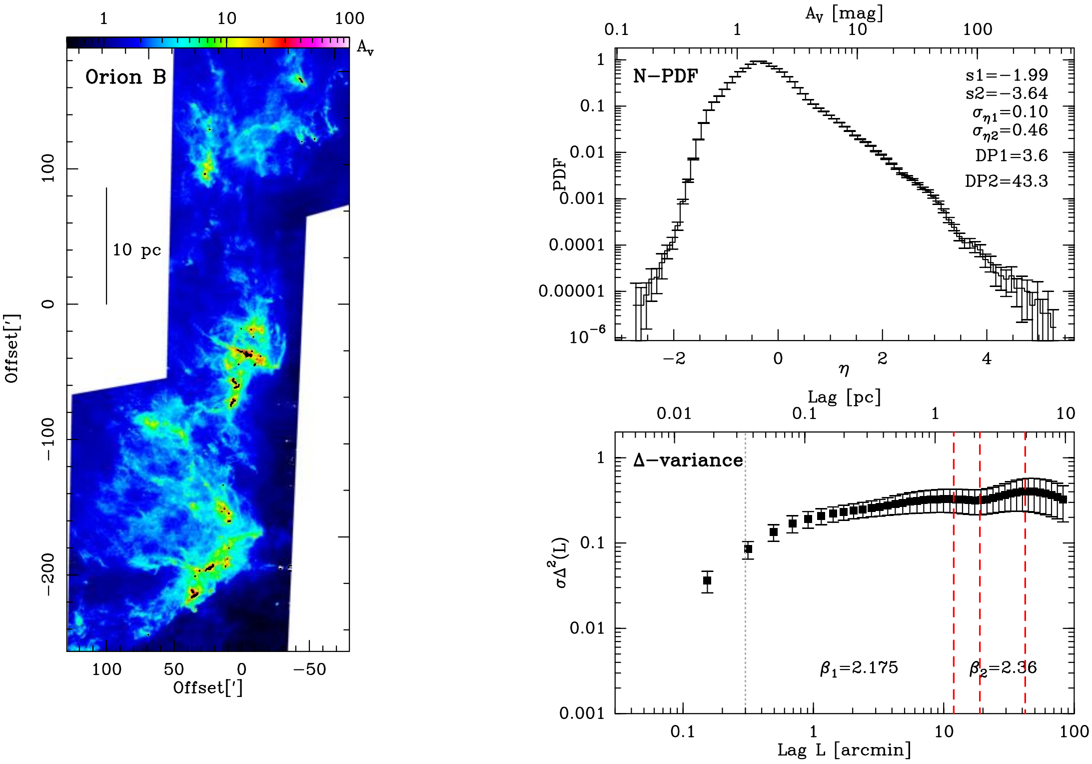

Fig. C.14: ORION-B: Fig. caption see Fig. C.1.

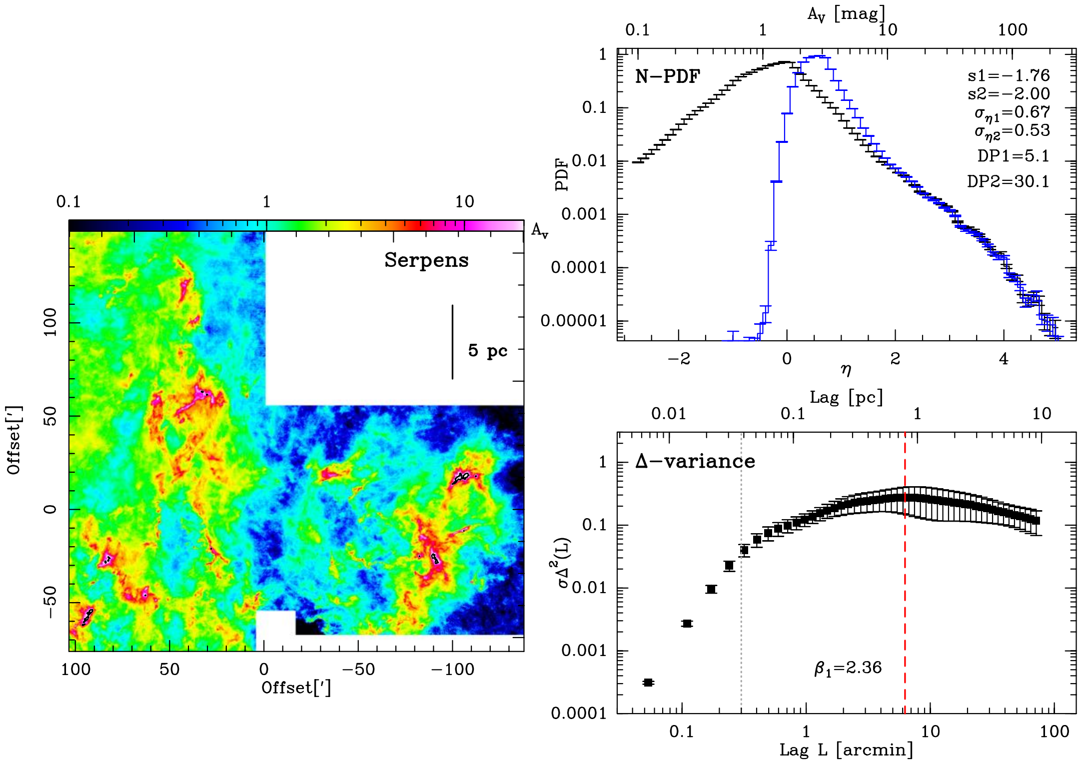

Fig. C.15: SERPENS: Fig. caption see Fig. C.1. For comparison, the N-PDF of the uncorrected map is displayed in grey.

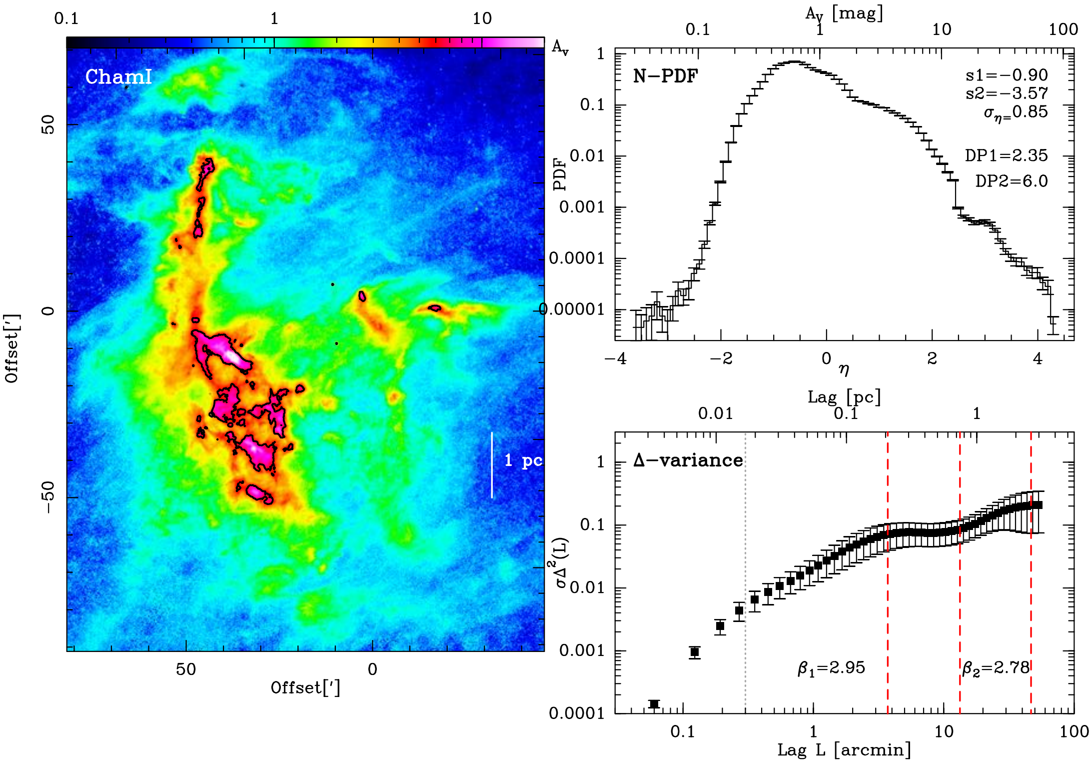

Fig. C.16: Chamaeleon I: Fig. caption see Fig. C.1.

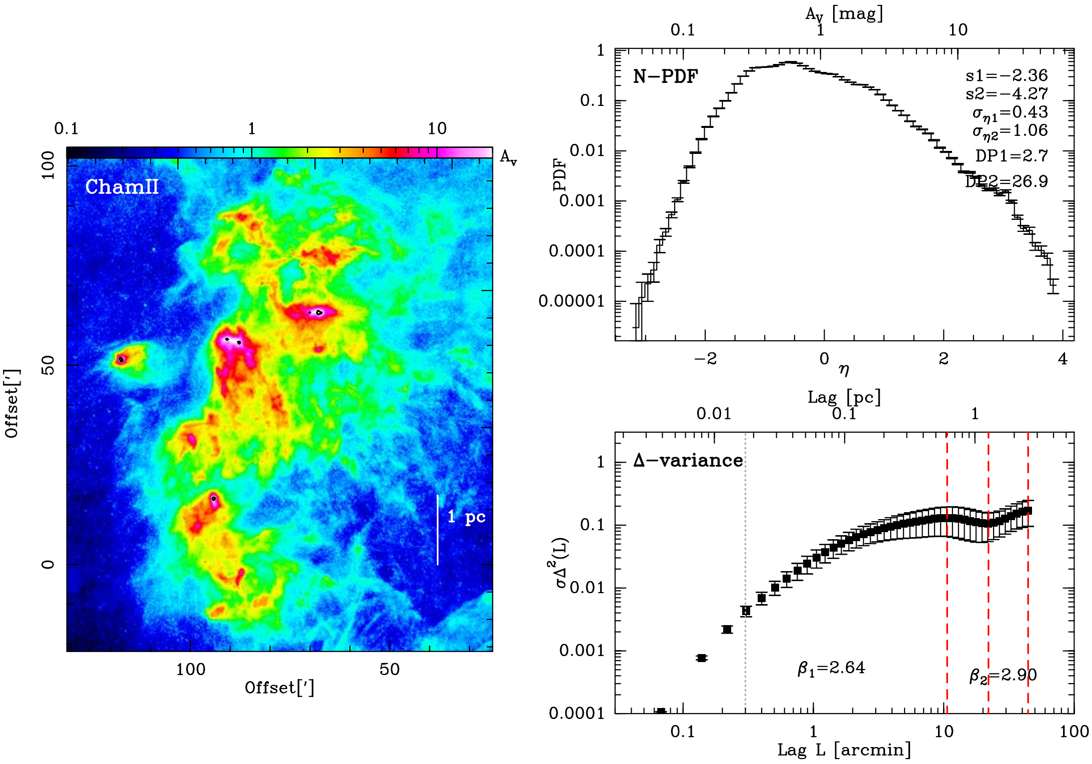

Fig. C.17: Chamaeleon II: Fig. caption see Fig. C.1.